Robotics and Autonomous Systems 145 (2021) 103843

Contents lists available at ScienceDirect

Robotics and Autonomous Systems

journal homepage: www.elsevier.com/locate/robot

Towards autonomous ergonomic upper-limb exoskeletons: A computational approach for planning a human-like path ☆

Rana Soltani Zarrin [a,*], Amin Zeiaee [a], Reza Langari [a,b], John J. Buchanan [c], Nina Robson [d]

[a] Department of Mechanical Engineering, Texas A&M University, College Station, TX, USA
[b] Department of Engineering Technology and Industrial Distribution, Texas A&M University, College Station, TX, USA
[c] Department of Health and Kinesiology, Texas A&M University, College Station, TX, USA
[d] Department of Mechanical Engineering, California State University, Fullerton, CA, USA

ARTICLE INFO

Article history:
Received 18 July 2020
Received in revised form 31 December 2020
Accepted 3 July 2021
Available online 24 July 2021

Keywords:
Computational models
Human-like motion
Path planning
Upper-limb exoskeletons
Scapulohumeral rhythm

ABSTRACT

Computational path planning approaches can enable development of autonomous rehabilitation and assistive exoskeletons. Using a human-like reference behavior for such wearable systems can ensure safe, effective, and intuitive human–robot interaction. This is of significant importance since the quality of interaction and ergonomic considerations have a substantial effect on technology usability and acceptance by the users. This paper proposes a novel framework for generating human-like paths for wearable exoskeletons in the shoulder-elbow level. The introduced method is a two-stage process where a human-like reference path is planned in the configuration space of the human arm, followed by an analytical transformation that directly maps the derived path to the configuration space of the exoskeleton. The analytical mapping presented is a function of the kinematic parameters of the system and can be adapted for other upper-limb exoskeletons. As a case study, the proposed method is used for generating human-like reference motions for a six-degree-of-freedom exoskeleton supporting scapulohumeral rhythm, glenohumeral rotations, and elbow flexion/extension. Firstly, it is shown that reaching motions associated with activities of daily living can be predicted with high accuracy in the human joint space. This is demonstrated by analyzing the experimental data collected from healthy subjects. Subsequently, it is verified through kinematic analysis that the transformation of generated paths to the exoskeleton configuration space does not alter their spatial profile in the task space.

1. Introduction

Upper-limb exoskeletons have proven to be a promising technology for assistive purposes, occupational applications, and rehabilitation of motor impairments [1,2]. In all these applications, achieving an intuitive and ergonomic interaction between the exoskeleton and the user is a critical criterion for usability, acceptance, and potentially the effectiveness of the system [3–5]. A core requirement for realizing such an interaction is the capability of the system in producing natural and human-like movements [6]. This is especially important for therapeutic exoskeletons where the robot has a more dominant role in controlling and correcting the motions of the limb based on a prescribed reference behavior [7,8]. Currently, therapists are responsible for devising the training motions, however, the effectiveness and autonomy of a robot-based therapy can be significantly improved by utilizing a human-like reference motion generation algorithm which can be adjusted based on individual patients' conditions (e.g. range of motion, spasticity level, etc.). It can be argued that such a feature can be very useful for assistive systems as well [9,10]. Human-like motion generation along with high-level intention detection algorithms are essential for achieving autonomous assistive technologies that can be integrated into the daily lives of the disabled.

Various methods have been used in the literature for reference motion generation of exoskeletons. Using the recorded motion of the affected limb moved by a therapist is a common approach. In this method, the motion of a healthy individual is recorded by a motion capture system [11,12], or by an exoskeleton attached to the patient and back-driven by the therapist [13]. In a similar approach, mainly used in bilateral systems, the motion of the healthy side of the patient can be mirrored on the affected side [14,15]. These methods necessitate the presence of a therapist to move the patient's arm to generate every motion or require additional equipment such as bilateral exoskeletons, motion capture systems, and a technician familiar with the equipment. These restrictions limit the application of exoskeletons to

☆ This work was supported in part by the Qatar National Research Fund under Grant NPRP No.: 7–1685–2 –626.
* Corresponding author.
E-mail address: rana.soltani@tamu.edu (R. Soltani Zarrin).

https://doi.org/10.1016/j.robot.2021.103843
0921-8890/

clinical settings rather than potential home-based options and increase the cost and complexity of the systems. To address the aforementioned limitations and to automate the path generation process, computational approaches could be used [16]. Computational models are grounded on theoretical studies on motion generation principles of the human Central Nervous System (CNS). The majority of these computational models use an optimization-based approach in accordance with the hypotheses that CNS plans the upper limb motions such that a specific cost is minimized. Motion jerk in task space [17–19], angular jerk [20], squared change of the joint torques [21,22], work done by joint torques [23], peak work [24], and energy [25] are examples of the cost functions studied in the literature.

Among the diverse sets of computational models, Minimum Jerk (MJ) in task space has been widely adopted for motion planning of upper-limb exoskeletons [17,18,26]. This can be partially attributed to the computational ease of planning motions in task space without the need to consider the specific kinematic and dynamic properties of the actual robot. However, due to the redundant nature of human arm kinematics, utilizing a task-space path planning strategy necessitates use of an additional algorithm for resolving redundancies. Another model used in the literature for exoskeleton motion planning is based on minimizing the squared derivative of joint trajectories [27]. This choice of the cost function results in minimum distance paths in the configuration space (MDC) and is therefore computationally very efficient. It should be noted that an MDC path in the configuration space (c-space) of an exoskeleton is not necessarily equivalent to the MDC path in the configuration space of the human arm model (except for exoskeletons whose shoulder joint axes align with the biologic axes of the human shoulder [28]). As a result, constructing a straight line between the initial and final poses of the exoskeleton does not always result in an MDC path for the human arm [11]. This issue prevents the direct use of computational models formulated in the c-space of the human arm for motion generation in exoskeletons.

This paper introduces a framework for solving the problem of human-like motion generation in upper-limb exoskeletons. The proposed framework is a two-stage process where a human-like reference path is generated in the configuration space of the human arm first. Supporting Scapulohumeral Rhythm (SR) and spatial similarity of the generated motions to the healthy motion patterns (in task space as well as human joint space) are the human-like qualities considered. To this end, first a computational model is developed by integrating inner shoulder models into the minimum kinetic energy path-generation algorithm in Riemannian space. The second stage involves transforming the generated path using an exoskeleton-specific transformation developed for mapping the c-space of the human arm to the exoskeleton's c-space. This mapping between the two spaces is derived using analytical geometry and is named Geometric Equivalence for Anthropomorphic Arms (GEAA). The proposed path generation approach is applied to a six degrees-of-freedom upper-limb exoskeleton (CLEVERarm [29]) which supports scapulohumeral rhythm, humeral rotations and elbow flexion/extension. To validate the effectiveness of the proposed GEAA transformation, it is shown that kinematic characterizations of the transformed trajectory and the outputs of the underlying computational model are equivalent. Additionally, through an experimental approach, it is shown that the outputs of the proposed framework bear a strong resemblance to the natural motions of the arm. It is important to note that the proposed method can be adapted for use on other upper-limb exoskeleton with different kinematic structure and supports the use of different computational models. This paper is organized as follows: Section 2 presents the terminology used and outlines the two-stage path generation algorithm in a conceptual level, Section 3 presents the motion planning in human configuration space, Section 4 demonstrates construction of the GEAA mapping for a six degree of freedom exoskeleton. The data collection procedure, simulation and experimental results, and quantitative analysis of the acquired data are presented in Section 5. Finally, Section 6 concludes the paper by reviewing the main contributions and findings of the paper.

Table 1
Nomenclature of the proposed framework.

Symbol	Description
$\boldsymbol{x}_w$	Wrist (hand) position
$\boldsymbol{x}_{GH}$	Glenohumeral joint center position
$\boldsymbol{q}_h$	Human arm configuration
$\boldsymbol{q}_e$	Exoskeleton configuration
$\boldsymbol{Q}_h$	Human arm configuration space
$\boldsymbol{Q}_e$	Exoskeleton configuration space
$\boldsymbol{e}_a$	Direction of the upper arm
$\boldsymbol{f}$	Forward kinematics function
$\boldsymbol{f}^{-1}$	Inverse kinematics function
$\boldsymbol{h}$	Inner shoulder model
$\boldsymbol{T}$	Transformation between configuration spaces
θ	Elevation of the arm
λ	Path parametrization variable
γ	Swivel angle
β	Geometric parameters of the exoskeleton

Table 2
List of acronyms.

Acronym	Full word
CNS	Central Nervous System
GH joint	Glenohumeral joint
SR	Scapulohumeral Rhythm
MDC	Minimum Distance path in C-space
GEO	Geodesic Curves
ADL	Activities of Daily Living
HPDI	Hand Path Deviation Index
RMSE	Root Mean Square Error

2. The proposed framework

The motion generation problem considered here focuses on the elbow-shoulder coordination. Additionally, the problem is formulated for the general case of upper-limb exoskeletons which do not necessarily have biologically matching shoulder axes and can include the inner shoulder motions as well. The nomenclature required for introducing the framework are presented in Table 1, where the bold-face font denotes vector quantities. Additionally, Table 2 presents a summary of the acronyms used throughout the paper.

Based on the introduced nomenclature, it is evident that the forward and inverse kinematics functions for the human arm model, $\boldsymbol{f}_h$ and $\boldsymbol{f}_h^{-1}$, satisfy the following equations:

$$\begin{aligned} \boldsymbol{x}_w &= \boldsymbol{f}_h(\boldsymbol{q}_h) \\ \boldsymbol{q}_h &= \boldsymbol{f}_h^{-1}(\boldsymbol{x}_w) \end{aligned} \tag{1}$$

Additionally, the inner shoulder model, $\boldsymbol{h}$, is a vector function which relates the elevation of the arm to the position of the Glenohumeral (GH) joint center:

$$\boldsymbol{x}_{GH} = \boldsymbol{h}(\theta) \tag{2}$$

Phase I — Generate a human-like motion profile

A computational model outputs a sequence of poses for the human arm model, which can be parametrized with a (unitless) scalar variable $\lambda \in [0, 1]$. Output motion profile of the computational model is defined as:

$$\Sigma_{Q_h} \triangleq \left\{ \boldsymbol{q}_h(\lambda) \in Q_h \,|\, \boldsymbol{q}_h(0) = \boldsymbol{q}_0, \boldsymbol{f}_h(\boldsymbol{q}_h(1)) = \boldsymbol{x}_f \right\} \tag{3}$$

where $\boldsymbol{x}_f$ and $\boldsymbol{q}_0$ are the final position of the hand and the initial configuration of the arm, respectively.

Phase II — Transform the motion profile to the configuration space of the exoskeleton

The objective sought is development of a transformation, $T(\boldsymbol{\beta}, \boldsymbol{h}) : Q_h \rightarrow Q_e$, which can be used to construct a task-space equivalent of Σ_{Q_h} in Q_e:

$$\Sigma_{Q_e} \triangleq \left\{ \boldsymbol{q}_e(\lambda) \in Q_e | \, \forall \lambda : \, \boldsymbol{q}_e(\lambda) = \boldsymbol{T}(\boldsymbol{q}_h(\lambda) \in \Sigma_{Q_h}) \right\} \tag{4}$$

such that

$$\forall \lambda : \quad \boldsymbol{f}_h(\boldsymbol{q}_h(\lambda) \in \Sigma_{\boldsymbol{Q}_h}) = \boldsymbol{f}_e(\boldsymbol{q}_e(\lambda) \in \Sigma_{\boldsymbol{Q}_e}) \tag{5}$$

The fundamental idea for the development of this transformation is that both systems (human arm model and exoskeleton), represent the same kinematic entity, i.e. directions of the upper arm and forearm, with different representations:

$$\boldsymbol{e}_a(\boldsymbol{q}_h) = \boldsymbol{e}_a(\boldsymbol{q}_e) \tag{6}$$

Thus, the two configuration spaces can be related to each other through a transformation. The GEAA method proposed in this paper employs the Denavit–Hartenberg (DH) convention to construct this mapping. In this method, the equivalence of upper arm and forearm directions when expressed in the same coordinate frame, along with the knowledge on the geometry of the exoskeleton is used to identify the loci of rotation axes for the exoskeleton joints. The rotation axes are then used to construct the DH coordinate frames and the configuration of the exoskeleton.

3. Human-like motion generation in human arm configuration space

Supporting the scapulohumeral rhythm and spatial similarity of the generated motions to the healthy motion patterns (in task space as well as human joint space) during three-dimensional large arm movements, such as Activities of Daily Living (ADL), are the desired human-like attributes considered in this work. Most upper-limb motions during the activities of daily living involve large ranges of movements and require elevation of the arm. Elevation of the arm results in the movement of the center of the Glenohumeral (GH) joint through the SR. Neglecting this motion in path generation and assuming the shoulder center to be fixed can result in joint misalignment between the exoskeleton and the human body, making the physical interaction uncomfortable for the user. To support the SR, the coupling between the inner shoulder motions and arm elevation needs to be integrated into the formulation of the computational model generating the arm motions. In this paper, a model relating the movements of the GH center and the arm elevation is developed and employed. The details of the model will be discussed at the end of this section. The underlying computational model used in this work is Geodesics in Riemannian space [25,30]. This approach is based on minimizing the kinetic energy of motion and therefore, incorporates inertial properties of the arm, believed to be important in path generation [30,31], within the planning algorithm. In this formulation, the kinetic energy of the motion is linked to the path length, making kinetic energy minimization equivalent to finding the minimum-length paths. Experimental studies involving healthy subjects have shown the success of geodesics compared to other models, such as minimum torque and minimum jerk, in modeling point-to-point reaching motions [25,32,33].

Fig. 1 illustrates the model of a human arm used in the formulation of the problem, where $\boldsymbol{q} = (\theta, \eta, \zeta, \varphi)$ denotes the configuration of the arm, and θ, η, ζ, φ represent elevation, azimuth, torsion angle of the shoulder, and flexion of the elbow,

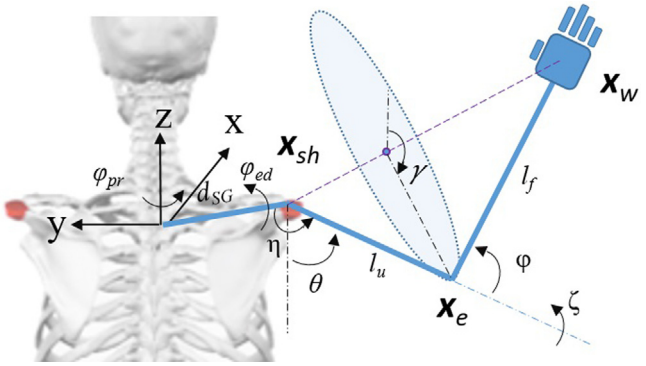

Fig. 1. Human arm model with inner shoulder.

respectively. In this model, azimuth (η) is defined as the angle of the projection of the arm on the x-y plane measured from the positive y axis. Moreover, $\boldsymbol{x}_w$, $\boldsymbol{x}_e$, and $\boldsymbol{x}_{sh}$ represent the wrist, elbow, and shoulder positions, respectively; whereas l_u and l_f are the upper-arm and forearm lengths. The DH parameters used to derive $\boldsymbol{f}_h$ and inverse kinematics mapping, $\boldsymbol{f}_h{}^{-1}$, for this arm model are included in Appendix A. For a Riemannian manifold $\boldsymbol{Q}$ with the metric $\boldsymbol{M}$ (mass-inertia tensor of the arm model), the geodesic path can be found by solving the following two-point boundary value problem, also known as the geodesic equation:

$$\begin{aligned} &\boldsymbol{M}(\boldsymbol{q}_h)\frac{d^2\boldsymbol{q}_h}{d\lambda^2} + \boldsymbol{C}(\boldsymbol{q}_h, \frac{d\boldsymbol{q}_h}{d\lambda})\frac{d\boldsymbol{q}_h}{d\lambda} = 0 \\ &\boldsymbol{q}_h(0) = \boldsymbol{q}_0, \boldsymbol{q}_h(1) = \boldsymbol{f}_h^{-1}(\boldsymbol{x}_w) \end{aligned} \tag{7}$$

where $\boldsymbol{M}$ and $\boldsymbol{C}$ denote the mas-inertia and Coriolis matrices. Definitions of these matrices and the derivation of the geodesic equation are discussed in Appendix B of the paper.

As (7) shows, solution of the geodesic equation depends on the final configuration of the arm. However, using inverse kinematics to determine $\boldsymbol{q}_h(1)$ is not straightforward and a redundancy resolution algorithm is needed due to the redundancy of the arm. Parametrization of all the inverse solutions using the swivel angle γ, as shown in Fig. 1, is a common approach to structure the problem [25]. Each γ value determines an elbow position, and therefore a unique inverse kinematics solution. Finally, solving the geodesic equation for each feasible γ value (i.e. final pose of arm), yields a family of geodesics. The redundancy resolution approach used is the minimization of the curve kinetic energy [25]:

$$\min_{\gamma} J = \frac{1}{2}\int_0^1 \mathbf{q}_h{}'(\lambda, \gamma)^T \mathbf{M}(\lambda, \gamma)\mathbf{q}_h{}'(\lambda, \gamma) d\lambda \tag{8}$$

Considering the scapulohumeral rhythm in arm motions adds another layer of complexity to the inverse kinematics problem. The increased complexity is due to the fact that the final configuration of the arm found through the inverse kinematics determines the position of the shoulder center, and the shoulder center position affects the solution of the inverse kinematics problem. Therefore, solving inverse kinematics problem requires finding the fixed-point of this interdependent relationship, given the range of motion constraints specific to each subject. To address this issue, this paper proposes an optimization-based approach where for each γ, inverse kinematics is solved as a constrained optimization problem formulated as follows:

$$\begin{cases} \min\limits_{q_h(1)} \boldsymbol{J} = \|\boldsymbol{q}_h(1) - \boldsymbol{f}^{-1}(\boldsymbol{x}_f - \boldsymbol{h}(\boldsymbol{q}_h(1)))\| \\ s.t. \ \boldsymbol{q}_h(1) \in \boldsymbol{q}_{h_{feasible}} \end{cases} \tag{9}$$

where $\boldsymbol{q}_{h_{feasible}}$ is the set of feasible configurations for the arm model, determined based on the achievable range of motion of

Table 3
Biologic joint limits.

	θ	η	ζ	φ
Max	π	$-\pi/6$	$\zeta_{ext}(\theta,\eta)$	π
Min	0	$-5\pi/4$	$\zeta_{int}(\theta,\eta)$	0

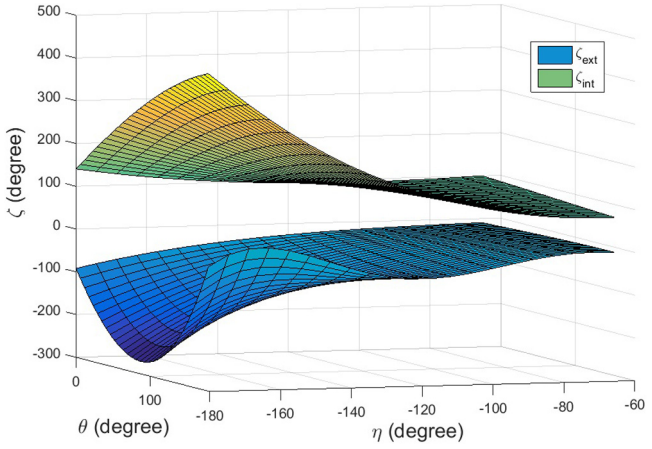

Fig. 2. Biological joint limits for internal and external rotations of the shoulder.

human upper extremity. The average feasible range of motion for healthy subjects are summarized in Table 3. It is important to note that biological limits for the internal and external rotations of the shoulder depend on the elevation and azimuth angles [34], and are demonstrated by two surfaces in Fig. 2.

To account for the shoulder center movement in the path planning problem, in this work an inner shoulder model is developed based on the recorded kinematic data of shoulder girdle movement during humeral elevation. This model describes the position of the GH joint center in spherical coordinates as follows:

$$\boldsymbol{h}(\theta) = \begin{bmatrix} d_{SG}\cos(\varphi_{ed})\cos(\varphi_{pr}) \\ -d_{SG}\cos(\varphi_{ed})\sin(\varphi_{pr}) \\ d_{SG}\sin(\varphi_{ed}) \end{bmatrix} \tag{10}$$

where the parameters used in this model are shown in Fig. 1. In this model, similar to [35], the elevation/depression inclination, φ_{ed}, is the angle between the projection of d_{SG} on the frontal plane during movement relative to its projection on the frontal plane in the reference position. Reference position is when the arm with relaxed shoulders is fully extended downwards by the side of the body and the palm is facing the body. Similarly, the protraction/retraction inclination, φ_{pr}, is the relative inclination of the projection of d_{SG} on the horizontal plane. Fig. 3 shows the captured data from 10 healthy subjects performing unilateral humeral elevation in the humeral reachable workspace on the frontal and sagittal planes and the two anterior planes located in 45° with respect to them. Vicon motion capture system and its reflective markers were used for tracking the motion of anatomical land-marks. Details of experimental protocol used for data collection are provided in Section 5. Following an empirical modeling approach, the function describing the inner shoulder motion is calculated as follows:

$$\begin{cases} \frac{d_{SG}}{d_0} = 9.3\times10^{-8}\theta^3 - 2.36\times10^{-5}\theta^2 - 4.21\times10^{-4}\theta + 1 \\ \varphi_{ed} = 4.34\times10^{-5}\theta^3 - 3.21\times10^{-3}\theta^2 + 0.1\theta - 0.06 \\ \varphi_{pr} = -5.28\times10^{-7}\theta^4 + 7\times10^{-5}\theta^3 - 3.92\times10^{-3}\theta^2 \\ +0.04\theta + 0.13 \end{cases} \tag{11}$$

where d_0 is the value of d_{SG} when $\theta = 0$. This parameter needs to be updated based on the body measurements of individual subjects.

4. Transformation of the generated motion to the exoskeleton c-space

This section outlines the derivation of GEAA for a six degree of freedom exoskeleton (CLEVERarm [29]) which supports scapulo-humeral rhythms, humeral rotations and elbow flexion/extension through actuated joints. The GEAA method at a conceptual level along with the DH coordinate frames needed to construct GEAA are shown in Fig. 4. With a known configuration of the arm, $\boldsymbol{q}_h$, forward kinematic equations can be used to determine the direction of the upper-arm, $\boldsymbol{e}_a$. Considering that the directions of upper-arm and forearm are the same between the two systems, analytical geometry techniques can be used to reconstruct the configuration of the exoskeleton.

Inner shoulder configuration is determined independently based on the inner shoulder model, $\boldsymbol{h}(\theta)$, and elevation of the arm (θ in $\boldsymbol{q}_h$). For the CLEVERarm, the rotation of the revolute joint 1 and translation of the prismatic joint 2 can be directly calculated from (11) , i.e, φ_{ed} and d_{SG}. For other exoskeletons with different inner shoulder design, inner shoulder configuration can be found by solving the inverse problem for the shoulder center data.

To construct the transformation for the shoulder degrees of freedom, upper-arm direction ($\boldsymbol{e}_a$) needs to be determined. Using forward kinematic equations, $\boldsymbol{f}_h$, the direction of upper-arm in the base coordinate system can be expressed as:

$$\boldsymbol{e}_a = [\sin\eta\sin\theta, \cos\eta\sin\theta, -\cos\theta] \tag{12}$$

With a known inner shoulder configuration, the axis of rotation of the first shoulder joint ($\boldsymbol{z_2}$) can be found as:

$$\boldsymbol{z}_2 = \boldsymbol{R}_2^0.\begin{bmatrix}0 & 0 & 1\end{bmatrix}^T \tag{13}$$

where $\boldsymbol{R}_2^0$ denotes the rotation matrix between base frame and frame 2. The locus of the rotation axis of the third shoulder joint ($\boldsymbol{z_4}$) is a cone resulting from the rotation of $\boldsymbol{z_4}$ around the upper-arm direction vector ($\boldsymbol{e}_a$), as shown with a red cone in Fig. 5. Let $\boldsymbol{\beta}$ denote the angle between the consecutive axes of rotation for shoulder mechanism. Using this parameter, the locus of the rotation axis of the third shoulder joint ($\boldsymbol{z_4}$) can be mathematically represented as an inner-product equation:

$$\langle \boldsymbol{z}_4, \boldsymbol{e}_a \rangle = \cos(\boldsymbol{\beta}(1)) \tag{14}$$

Based on the DH coordinate assignment, $\boldsymbol{z}_4$ is co-located on a plane formed by the axis of rotation of elbow, $\boldsymbol{z}_5$, and $\boldsymbol{e}_a$. This plane is denoted by P_1 in Fig. 5, and can be defined by its normal vector, $\boldsymbol{n}$, which can be determined as follows:

$$\boldsymbol{n} = \boldsymbol{e}_a \times \boldsymbol{z}_5 \tag{15}$$

The rotation axis of the elbow, $\boldsymbol{z}_5$, used in the above equation can be directly determined by the internal/external rotation of the shoulder, ζ. The intersection of the conic locus of $\boldsymbol{z}_4$ with the P_1 plane determines the rotation axis of $\boldsymbol{z}_4$. Thus, $\boldsymbol{z}_4$ can be found by solving the following second-order algebraic equations:

$$\begin{cases} \langle \boldsymbol{z}_4, \boldsymbol{n} \rangle = 0 \\ \langle \boldsymbol{z}_4, \boldsymbol{e}_a \rangle = \cos(\boldsymbol{\beta}(1)) \\ \|\boldsymbol{z}_4\| = 1 \end{cases} \tag{16}$$

With known $\boldsymbol{z}_2$ and $\boldsymbol{z}_4$ axes, $\boldsymbol{z}_3$ can be determined by intersecting the two conic loci formed by rotation of $\boldsymbol{z}_3$ around $\boldsymbol{z}_2$ and $\boldsymbol{z}_4$. Fig. 6 shows these loci where the blue cone is created by the rotation of $\boldsymbol{z}_3$ around $\boldsymbol{z}_2$ axis, and the green cone is formed by rotation of $\boldsymbol{z}_3$ around the $\boldsymbol{z}_4$ axis. The procedure of identifying

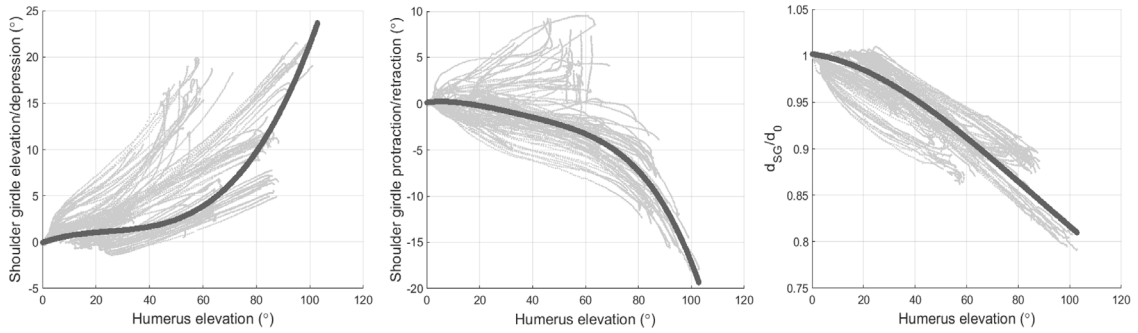

Fig. 3. Model describing the motion of shoulder girdle (a) elevation/depression, (b) protraction/retraction, (c) length change by humerus elevation..

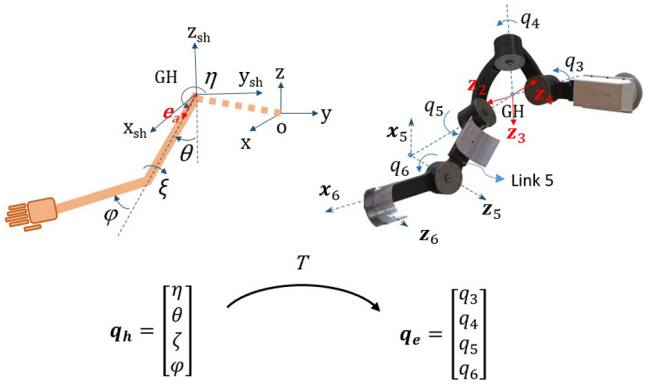

Fig. 4. Configuration spaces of the exoskeleton and human arm..

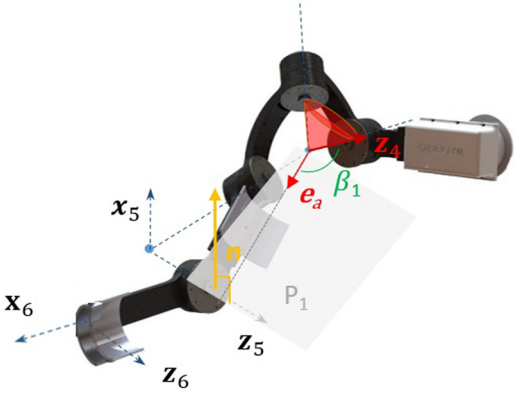

Fig. 5. Locus of 3rd shoulder joint.

z_3 is mathematically equivalent to solving the following set of equations:

$$\begin{cases} \langle z_2, z_3 \rangle = \cos(\beta(2)) \\ \langle z_4, z_3 \rangle = \cos(\beta(3)) \\ \|z_3\| = 1 \end{cases} \tag{17}$$

As mentioned earlier, the β parameters in Eqs. (16) and (17) represent the angle between the consecutive axes of rotation for shoulder mechanism. The generality of this set of equation therefore enables adopting the proposed approach for other exoskeletons with different shoulder design. For CLEVERarm, the vector of geometric parameters β is:

$$\beta = \begin{bmatrix} 125 & 70 & 100 \end{bmatrix} \tag{18}$$

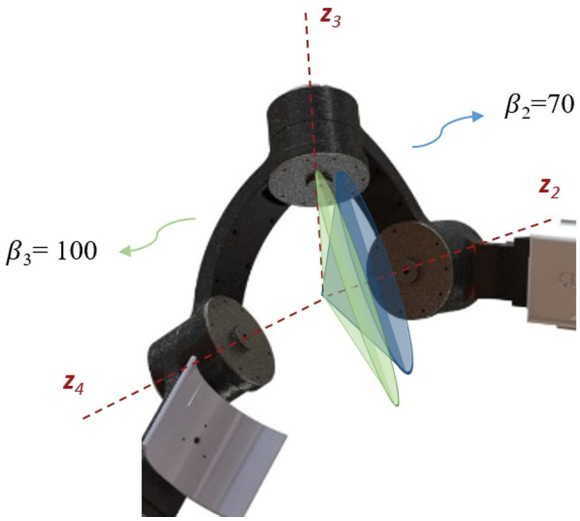

Fig. 6. Geometric representation of loci of 2nd shoulder joint.

The direction of each joint's axes of rotation, i.e. z_i, can be used for reconstructing the DH chain, i.e. x_i and y_i for individual frames. The x axes for the second and third shoulder joints as well as for the elbow can be found based on the DH coordinate convention which requires every x_i to be perpendicular to z_{i-1} and z_i, i.e.,

$$\begin{cases} x_3 = z_2 \times z_3 \\ x_4 = z_3 \times z_4 \\ x_5 = z_5 \times z_4 \end{cases} \tag{19}$$

Additionally, x_2 can also be calculated directly using the rotation matrix R_2^0 as follows:

$$x_2 = R_2^0 . \begin{bmatrix} 1 & 0 & 0 \end{bmatrix}^T \tag{20}$$

Configuration of the exoskeleton, i.e. q_e, can be found based on the angle between the x axes of consecutive DH frames. Additionally, the direction of rotation (i.e. sign of rotation angles), can be determined by direct substitution, i.e., a rotation of q_i degrees about z_i axis should transform x_{i-1} to x_i.

$$|q_i| = \frac{\langle x_{i-1}, x_i \rangle}{\|x_{i-1}\| \, \|x_i\|} \tag{21}$$

Finally, the transformation for the elbow joint between the two spaces is trivial as shown in Fig. 4:

$$q_6 = \frac{\pi}{2} - \varphi \tag{22}$$

Table 4
Marker names and locations on body.

Symbol	Marker location
SJN	Sternum Jugular Notch
CV7	Cervical Spine Vertebra 7
RCAJ	Right Clavicle-Acromion Joint
RHGT	Right Humerus Greater Tubercle
RHLT	Right Humerus Lesser Tubercle
RHLE	Right Lateral Epicondyle of Humerus
RHME	Right Medial Epicondyle of Humerus
RRSP	Right Radius-Styloid Process
RUSP	Right Ulna-Styloid Process

The computational cost of the proposed transformation is equivalent to solving two quadratic equations, i.e. (16) and (17). The alternative approach for constructing an angular path in the c-space of the exoskeleton which is equivalent to the output of the computational model, involves solving inverse kinematics problem. However, the method proposed in this paper is more efficient and less complex than the standard approaches for numerically solving the set of coupled nonlinear equations arising in inverse kinematics problem. It is noteworthy that GEAA can in fact be used as a stand-alone algorithm for solving inverse kinematics problem for upper-limb exoskeletons [36].

5. Simulation and experimental results

To develop the inner shoulder model, shoulder girdle kinematic data of healthy subjects performing unilateral arm motions were recorded using a motion capture system. Additionally, to evaluate the effectiveness of the proposed motion generation method, motions of healthy subjects performing a class of ADL motions were captured with the same system and compared with the algorithm outputs. The motion capture system used consisted of three 2.2 Megapixel Vicon optical camera (330 frames per second at full frame) and reflective markers. For solving the Geodesic equations MATLAB's (The MathWorks Inc.) built-in solver for boundary value problems (4th order method) was employed. Similar to any other boundary value problem, the choice of initial conditions has an immense impact on the convergence of the numerical solver. A multi-start approach was used in this work to minimize the effect of initial guess on the simulation results as much as possible.

5.1. Experimental protocol

Ten right-handed healthy subjects (2 female and 8 male) with an average age of 31 years (standard deviation of 5 years) with no history of upper-limb impairments voluntarily took part in the experiments. The experimental protocol was reviewed and approved by the Texas A&M IRB board (IRB 2016-0387D) prior to the experiments. Informed consent was received from every subject. For each subject, weight, height, upper-body dimensions including the clavicle length, and limb dimensions were measured. Before each experiment, the movements needed to be performed by the participants, initial and final points for each movement, and the general guidelines such as no trunk movement were explained. Using two-sided adhesives, nine reflective markers were attached to the subjects' skin according to a standard marker placement method (Visual3D^{TM} Modeling) as shown in Fig. 7 and Table 4, with SJN showing the origin of the reference coordinate system. Shoulder center was determined as the centroid of the 3 markers on the shoulder.

Subjects were asked to perform 4 types of ADL motions: reaching (to points located at two different heights), reaching to the mouth (drinking/eating), reaching to the head (combing), and reaching to the opposite side of the body (washing body). The starting point and wrist orientation for the motions were fixed for all the subjects, and the initial and final points for each movement were marked by colored labels. Final points, except for the reaching motions, were slightly different due to the individual body height and size differences and natural variations of human motions. Subjects were asked to repeat each motion 30 times, so a total of 1200 trials were performed. Fig. 8 shows one of the subjects performing the motions.

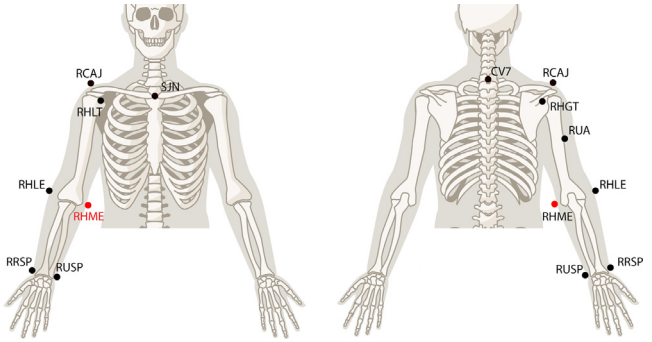

Fig. 7. Marker placement (red marker is used for calibration). (For interpretation of the references to color in this figure legend, the reader is referred to the web version of this article.)

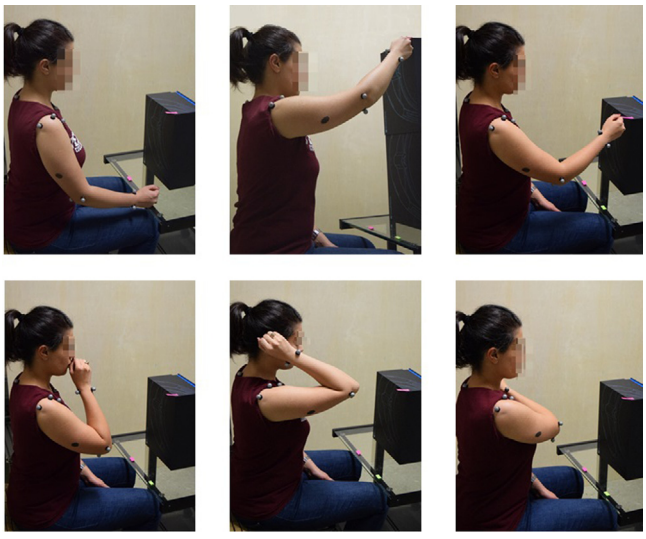

Fig. 8. ADL motions performed by a subject. Left most figure on the top shows the starting point of the movements, marked by a green label. (For interpretation of the references to color in this figure legend, the reader is referred to the web version of this article.)

5.2. Results and discussions

Figs. 9 and 10 present a comparison between the randomly selected experimental data captured from different subjects and the corresponding outputs of the proposed framework in task and joint levels. Solid blue lines represent the experimental data, while the green dashed graphs show the geodesic model outputs. Task-level comparisons are expressed in the human arm base coordinate system, while joint level comparisons are in the c-space of the human arm (Phase I outputs of the algorithm). To illustrate the importance of the underlying computational model in generating human-like motions, in addition to using geodesics in phase I, the proposed framework was also simulated with MDC

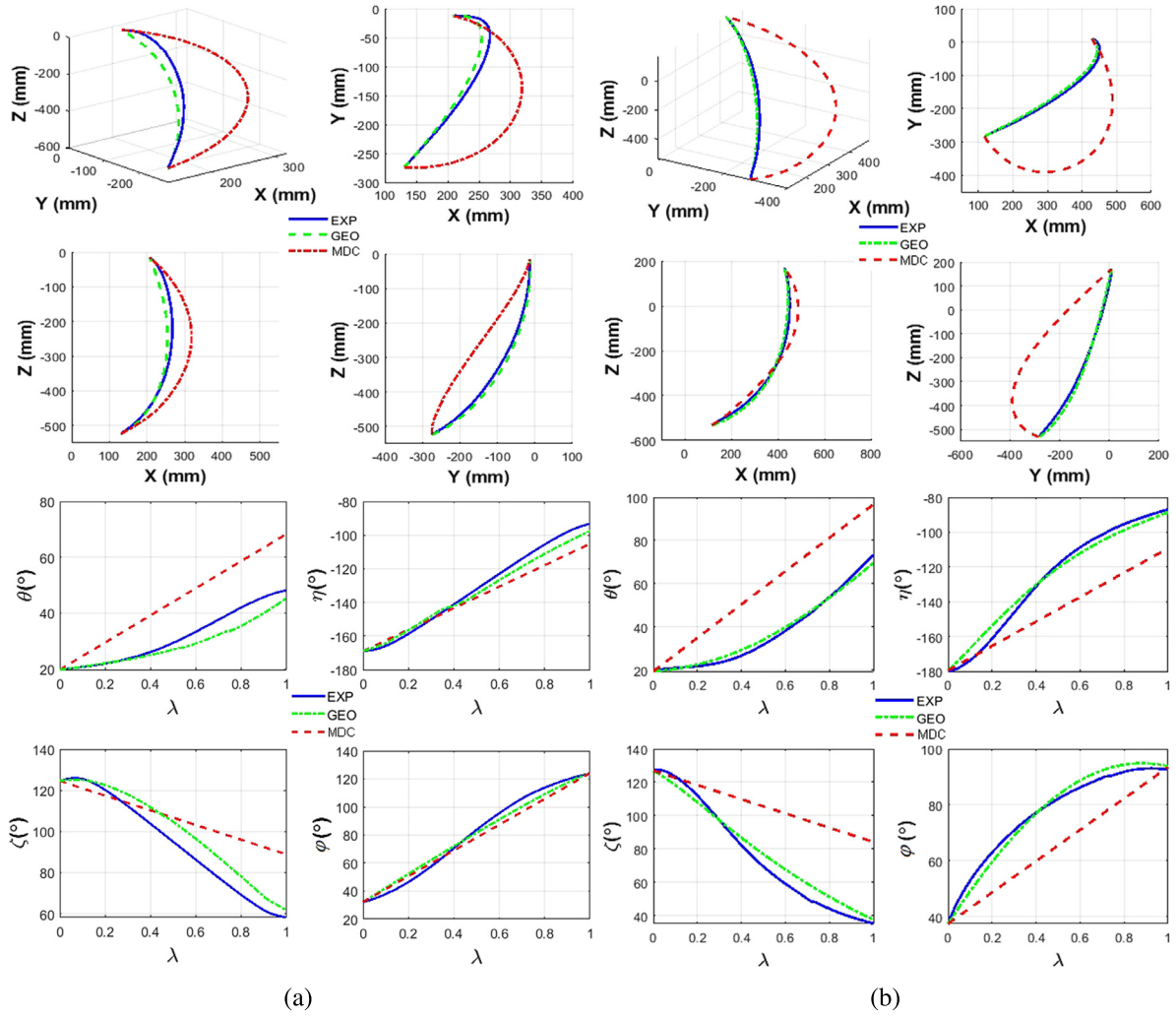

Fig. 9. Typical examples showing the comparison between randomly selected experimental data (- blue) and computational outputs (- - green for geodesics, and -. red for MDC models) for (a) eating and (b) reaching motions. For each motion, upper row shows the task level data, while the lower row presents the arm pose comparison (Phase I outputs).

Table 5
Task space quantitative measures: mean (± standard deviation).

		RMSE	*HPDI*
Eating	GEO	0.0801 (±0.0185)	0.1085 (±0.0238)
	MDC	0.0961 (±0.0168)	0.1397 (±0.0228)
Reaching	GEO	0.0153 (±0.0021)	0.0215 (±0.0034)
	MDC	0.1922 (±0.0171)	0.2671 (±0.0250)
Combing	GEO	0.1291 (±0.0197)	0.1779 (±0.0270)
	MDC	0.1942 (±0.0117)	0.2745 (±0.0158)
Washing	GEO	0.1225 (±0.0215)	0.1866 (±0.0341)
	MDC	0.1445 (±0.0337)	0.1965 (±0.0466)

computational model. Paths generated by the MDC model are presented by red dash-dotted graphs in Figs. 9 and 10.

To quantify the similarity between the generated paths and the experimental data, in addition to root mean square of the error (normalized by the motion length), the coefficient of determination (r^2), and the Hand Path Deviation Index (HPDI) values were calculated. HPDI is a non-negative index, with higher values showing less resemblance, which is defined as the absolute value of the maximum task-space error normalized by the distance between the initial and final hand positions, L, [25]. Let $\Sigma_{exp}(\lambda)$ and $\Sigma_{comp}(\lambda)$ denote the experimental and computational task-space motion profiles where λ denotes the path parametrization index. To quantify the similarity of two paths, HPDI can be defined as follows:

$$\text{HPDI} = \max_{\lambda} \frac{||\Sigma_{exp}(\lambda) - \Sigma_{comp}(\lambda)||_2}{L} \tag{23}$$

For the 4 classes of motions for all the subjects, Table 5 presents the quantitative comparison between the 3D experimental hand paths and the corresponding paths generated by the proposed framework using geodesics and MDC as the underlying computational models. Table 6 shows the similarity of the same paths when projected on the transverse, sagittal, and frontal planes of the body. Similarly, Table 7 summarizes the quantitative comparison between the experimental and computationally generated joint space paths, whereas Fig. 11 evaluates the overall

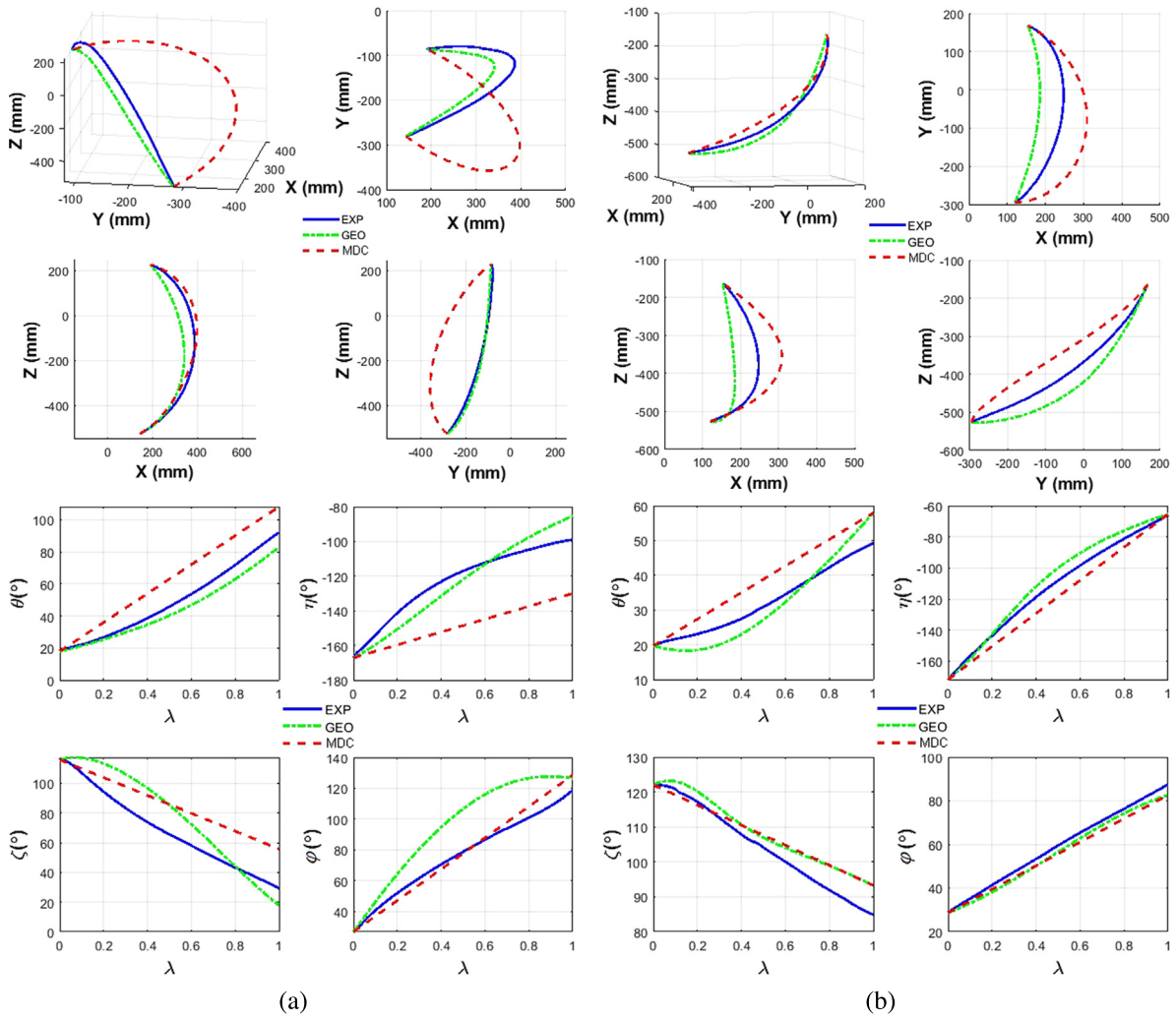

Fig. 10. Typical examples showing the comparison between randomly selected experimental data (- blue) and computational outputs (- - green for geodesics, and -. red for MDC models) for (a) combing and (b) washing motions. For each motion, upper row shows the task level data, while the lower row presents the arm pose comparison (Phase I outputs).

similarity of the computationally generated angular paths to the experimental data across different subjects and tasks using a scatter plot and the coefficient of determination associated with it.

As the results show, our proposed method using geodesics can in general generate motions with higher similarity to human actual arm motions compared with other common methods like MDC. The superiority of geodesics over MDC is more notable in outward motions (i.e. reaching) as opposed to inward motions (i.e. eating, washing and combing). However, when task-space similarity indices are studied for 2D projections of the paths on anatomical planes, the advantages of geodesics are less obvious. While geodesics have a higher resemblance to the experimental data when considered on transverse plane, they fall behind MDC on sagittal plane for inward motions. Similarly in the configuration space, ζ has the smallest similarity index as shown in Table 7, which is consistent with observations in [25]. These types of prediction errors could be due to the numerical complexity of solving boundary value problems describing geodesic paths, natural variations in scapulohumeral rhythm across different people, modeling challenges associated with accurate determination of the human arm inertial properties and range of motion, or the unwitting change of subject's wrist orientation which transpires in complex motions involving large and interconnected motions of shoulder and elbow. Further investigations on these observations, as well as path planning considering the orientation of the hand to account for object grasping, which is particularly important in activities of daily living, are parts of our future work. The observed discrepancies could also indicate that complex arm motions generated by the CNS might not be solely governed by minimum energy or minimum length path principles. This conclusion is inspired by our observation that the minimum energy paths are not necessarily the paths closest to the actual movement, although there is correlation between the path energy and its similarity to the experimental data. Fig. 12 is an example illustrating an eating motion trial in our study. The gray paths are the family of geodesic curves computed for different swivel angles. As shown in this example plot, the orange paths have the highest similarity to the blue experimental data, but are different from the minimum energy paths shown in green. This observation suggests the possibility that in performing complex arm motions, CNS selects paths based on a combination of different criteria, one of which is the energy minimization. The aforementioned numerical and experimental inaccuracies are the other potential explanation. Further studies are needed for understanding these observations better.

As another contribution of this paper, the effect of incorporating scapulohumeral rhythm in the motion planning algorithm is presented in Fig. 13. The plot illustrates the distribution of

Table 6
Quantitative comparison of task-space paths on transverse, sagittal, and frontal planes: HPDI mean (± standard deviation).

		Transverse plane	Sagittal plane	Frontal plane
Eating	GEO	0.0522 (±0.0152)	0.1004 (±0.0213)	0.1051 (±0.0229)
	MDC	0.1323 (±0.0182)	0.0584 (±0.0213)	0.1342 (±0.0225)
Reaching	GEO	0.0170 (±0.0013)	0.0206 (±0.0042)	0.0194 (±0.0065)
	MDC	0.2619 (±0.0269)	0.0897 (±0.0092)	0.2613 (±0.0248)
Combing	GEO	0.0820 (±0.0184)	0.1618 (±0.0375)	0.1644 (±0.0387)
	MDC	0.2716 (±0.0163)	0.0600 (±0.0067)	0.2686 (±0.0159)
Washing	GEO	0.0910 (±0.0162)	0.1437 (±0.0494)	0.1284 (±0.0435)
	MDC	0.1158 (±0.0278)	0.0900 (±0.0257)	0.1274 (±0.0320)

Table 7
Joint space quantitative measures: mean (± standard deviation).

			θ	η	ζ	φ
Eating	GEO	r^2	0.9913(±0.0064)	0.9898(±0.0087)	0.9553(±0.013)	0.9889(±0.0048)
		RMSE	5.8392(±2.6970)	3.5220(±1.6044)	8.8765(±3.5743)	4.5932(±1.1619)
	MDC	r^2	0.9536(±0.0132)	0.9853(±0.0042)	0.9617(±0.0040)	0.9880(±0.0021)
		RMSE	28.0471(±2.9024)	8.5952(±1.7709)	19.6788(±2.9644)	3.9236(±0.7046)
Reaching	GEO	r^2	0.9921(±0.0085)	0.9951(±0.0039)	0.9915(±0.0062)	0.9945(±0.002)
		RMSE	3.5756(±2.4005)	3.3882(±1.1592)	6.4681(±3.6797)	2.9158(±0.4129)
	MDC	r^2	0.9352(±0.0181)	0.9602(±0.0188)	0.9633(±0.0224)	0.8538(±0.0800)
		RMSE	21.0414(±3.2232)	12.4364(±1.6798)	23.6307(±3.2256)	16.4067(±4.1101)
Combing	GEO	r^2	0.9903(±0.0103)	0.9387(±0.0171)	0.9056(±0.0629)	0.9307(±0.0168)
		RMSE	5.3974(±1.7354)	9.8451(±2.9553)	11.8601(±4.6898)	10.8771(±2.1398)
	MDC	r^2	0.9827(±0.0039)	0.9108(±0.0213)	0.9303(±0.0066)	0.9840(±0.0036)
		RMSE	9.4531(±1.7727)	25.2989(±1.8284)	11.6682(±1.3493)	3.6770(±0.4306)
Washing	GEO	r^2	0.9635(±0.0334)	0.9925(±0.0056)	0.9013(±0.0841)	0.9863(±0.0089)
		RMSE	9.7326(±4.1496)	3.2676(±1.5024)	13.2444(±5.7077)	3.5632(±1.1844)
	MDC	r^2	0.9690(±0.0934)	0.9810(±0.0084)	0.9174(±0.0922)	0.9663(±0.0022)
		RMSE	9.4665(±3.3309)	5.1431(±1.3139)	14.7174(±4.8001)	3.8732(±1.6078)

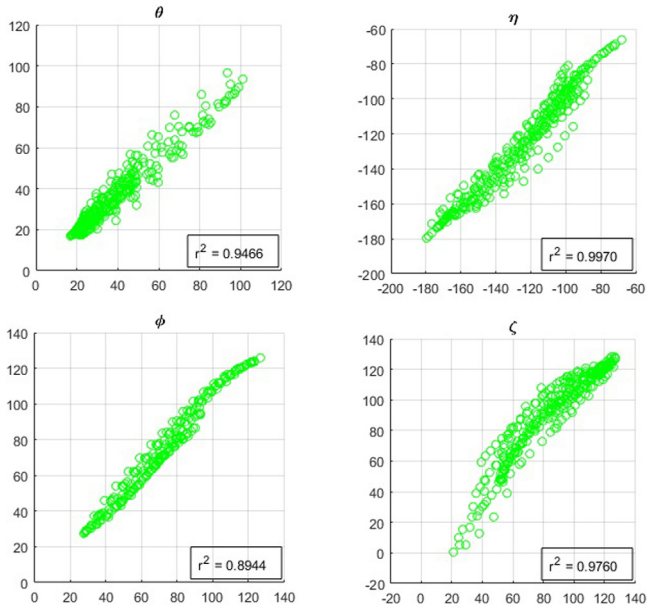

Fig. 11. Scatter plots comparing experimental data and geodesic model outputs in configuration space of the arm. Angles are in degree.

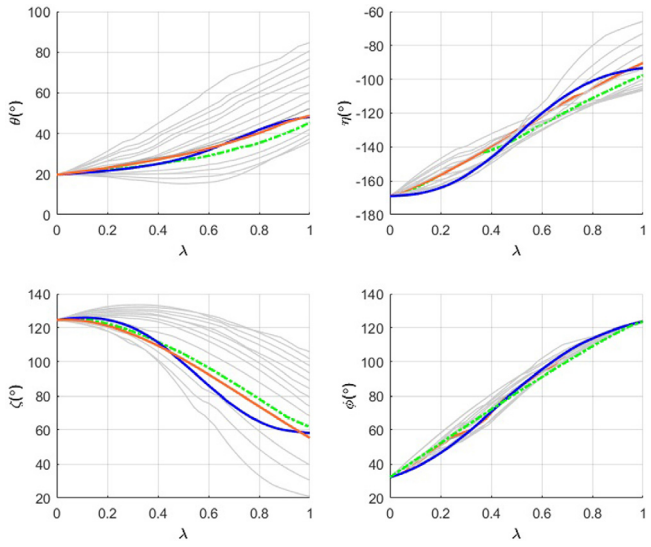

Fig. 12. Family of geodesic paths associated with different final configurations of the arm (i.e. different swivel angles). Minimum energy paths (green) do not necessarily correspond to the paths with highest similarity (orange) to the actual movements (blue). (For interpretation of the references to color in this figure legend, the reader is referred to the web version of this article.)

maximum misalignment in each trial across all the trials performed by all the subjects for each task. As shown in this bar-plot, incorporating inner shoulder model into the path planning algorithm reduces the misalignment between the predicted and actual shoulder center by %55.53 in average. This improvement is especially significant in motions involving larger elevations of the arm such as combing and washing. Reduced misalignment in motion generation can certainly improve the ergonomics of exoskeletons.

Finally, as mentioned before, derivation of the GEAA transformation is based on the equivalence of the actual and transformed motion profiles in the task space. This claimed task-space equivalence of the two paths is investigated by comparing the forward kinematic outputs of both systems when fed with their associated motion profiles. Fig. 14 shows the output of the computational

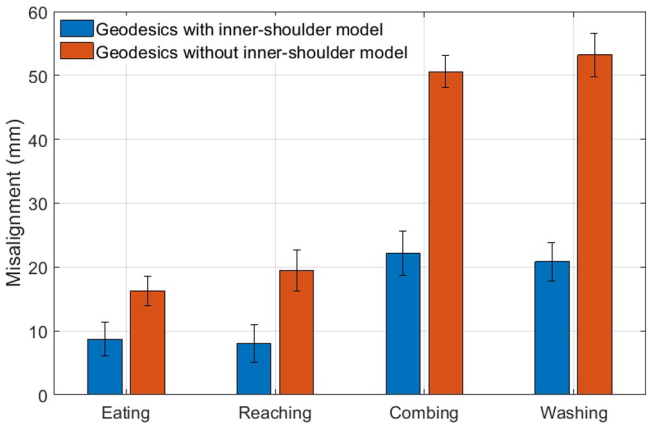

Fig. 13. Improvement in the shoulder center alignment through the inclusion of inner shoulder movements in the path planning algorithm using the proposed computational model.

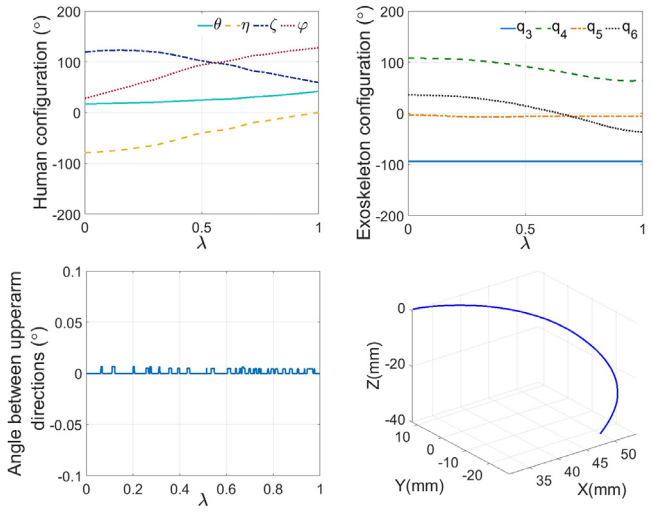

Fig. 14. Comparison between the configuration data in the c-space of the human arm and the equivalent configurations in the exoskeleton after GEAA transformation.

model for an eating motion in top left, while the equivalent transformed motion to the exoskeleton joint space using GEAA is depicted in top right. Calculating the upper-arm directions based on the resultant configuration space data verifies that both models represent the same upper-arm direction throughout the motion, as shown in the lower left sub-figure in Fig. 14. The very small differences observed are the result of the numerical errors in solving the algebraic equations in the transformation. Additionally, as presented in the lower right sub-figure, both motion profiles result in the same hand path, verifying that the transformation does not alter the spatial profile of the motion in the task space.

The proposed transformation has significant importance for computational models formulated in the configuration space of the arm. This is especially important for upper-limb exoskeletons with non-biological shoulder axes, since direct employment of human-arm-based c-space computational models is not possible as explained in Section 1. To demonstrate this limitation, MDC computational model is used to generate motions in the human arm and exoskeleton c-spaces for a horizontal abduction arm motion. The resulted minimum distance path in $\boldsymbol{Q}_h$ is compared with the minimum distance path between equivalent initial and

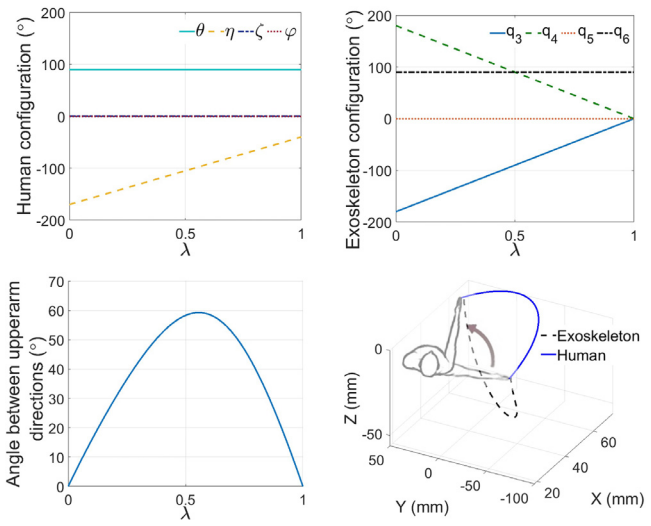

Fig. 15. Comparison between the configuration data in the c-spaces of human arm and the exoskeleton using MDC.

final configurations in $\boldsymbol{Q}_e$. The sub-figures on the top in Fig. 15 show the two MDC paths. To evaluate whether the two joint-space paths are task-space equivalent, the upper arm directions generated by the two paths are compared in the bottom left sub-figure. Additionally, hand paths generated by the two MDCs are presented in the bottom right sub-figure where the blue line and the black dashed line show the hand paths generated from the forward-kinematic analysis of the MDC in the human arm and exoskeleton configuration spaces respectively. As the two bottom sub-figures show, the two MDC trajectories are not equivalent in the task space. In other words, this result demonstrates that constructing a straight line between the initial and final poses of the exoskeleton does not result in a minimum-distance path for the human arm [11] and vice versa. As a result, planning paths in the c-space of the exoskeleton using methods developed based on the studies of human arm motions (such as the commonly used minimum angular jerk method), does not result in human-like motions for exoskeletons with non-biologic axes of rotation in shoulder.

6. Conclusion

This paper introduced a novel method for human-like path planing in upper-limb exoskeletons which support inner shoulder motions as well. This is achieved by incorporating empirical models describing scapulohumeral rhythm into the human arm path planning problem and transforming the resultant path to the configuration space of the exoskeleton using an analytical transformation. The application of the proposed framework on a six-degree-of-freedom robot is thoroughly discussed in this paper. The proposed method is capable of successfully generating upper-limb motions that have high resemblance to the actual arm motions. Since the developed transformation does not alter the spatial profile of the input motion in task space, any differences between the generated and actual motions originate from the underlying computational model (phase I of the proposed method). This observation highlights the importance of using accurate computational models in phase I to enhance the human-like nature of the generated motions. Choosing geodesics over other common computational approaches such as minimum-distance paths in c-space is a step in this direction. The proposed framework in this work enables using any computational model that can accurately predict the motion profile of the human arm

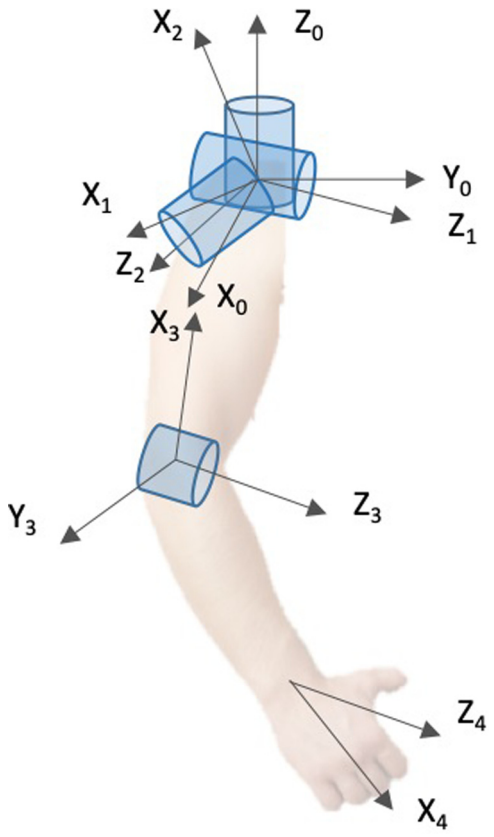

Fig. 16. DH coordinate assignment for the human arm model.

for motion planning of the exoskeletons. Similarly, the analytical transformation used in phase II of the algorithm can be adapted to other exoskeletons with different kinematic designs. Finally, the developed framework is computationally efficient compared with methods relying on numerical solution of inverse kinematics problem.

Declaration of competing interest

The authors declare that they have no known competing financial interests or personal relationships that could have appeared to influence the work reported in this paper.

Appendix A

By assigning the DH coordinate systems for the human arm model as depicted in Fig. 16, DH parameters for deriving the forward kinematics function, $\boldsymbol{f}$, are presented in Table 8. The inverse kinematics function, $\boldsymbol{f}_h^{-1}$, of the human arm model can be found as:

$$\begin{cases} \theta = cos^{-1}(-\dfrac{z_e}{l_u}) \\ \eta = atan2(-x_e, y_e) \\ \zeta = atan2(l_u(x_e y_w - x_w y_e), y_e(y_e z_w - y_w z_e) \\ \quad - x_e(z_e x_w - z_w x_e)) \\ \phi = cos^{-1}(\dfrac{x_w^2 + y_w^2 + z_w^2 - l_u^2 - l_f^2}{2 l_u l_f}) \end{cases} \tag{24}$$

where $atan2(.,.)$ denotes the four quadrant inverse tangent function.

Table 8
DH parameters of the arm model.

	a	α	d	θ
Shoulder Azimuth	0	-90	0	$\eta + 90$
Shoulder Elevation	0	-90	0	$-\theta$
Humeral Rotation	0	90	l_u	$-\zeta$
Elbow Flexion	l_f	0	0	$90 - \phi$

Appendix B

For a Riemannian manifold $\boldsymbol{Q}$ with the metric tensor g, a geodesic is the solution of the following 2nd order ordinary differential equation, also known as the geodesic equation:

$$g_{ij}\frac{d^2\boldsymbol{q}_h^j}{d\lambda^2} + c_{ijk}\frac{d\boldsymbol{q}_h^i d\boldsymbol{q}_h^k}{d\lambda d\lambda} = 0 \tag{25}$$

where $\boldsymbol{q}_h$ denotes the vector of the generalized coordinates representing a point in the Riemannian space, g_{ij} is the ith row and jth column elements of the metric tensor g, $d\boldsymbol{q}$ is the displacement element in the configuration space, and λ is the path parametrization variable. Additionally, c_{ijk} denotes the Christoffel symbols defined as:

$$c_{ijk} = \frac{1}{2}\left(\frac{\partial g_{ij}}{\partial \boldsymbol{q}_h^k} + \frac{\partial g_{ik}}{\partial \boldsymbol{q}_h^j} - \frac{\partial g_{kj}}{\partial \boldsymbol{q}_h^i}\right)\frac{d\boldsymbol{q}_h^k}{d\lambda}, \quad i = 1...., n \tag{26}$$

By choosing the inertia matrix of the arm as the Riemannian metric, i.e., $g(\boldsymbol{q}_h) = \boldsymbol{M}(\boldsymbol{q}_h)$, the nonlinear ordinary differential equation of (25) can be rewritten as (7), in which

$$\boldsymbol{M}_{ij}(\boldsymbol{q}_h) = \frac{\partial k(\boldsymbol{q}_h, \dot{\boldsymbol{q}}_h)}{\partial \dot{\boldsymbol{q}}_h^i \partial \dot{\boldsymbol{q}}_h^j} \tag{27}$$

where k denotes the kinetic energy of the arm.

References

[1] R. Gopura, D. Bandara, K. Kiguchi, G.K. Mann, Developments in hardware systems of active upper-limb exoskeleton robots: A review, Robot. Auton. Syst. 75 (2016) 203–220.
[2] J. Theurel, K. Desbrosses, Occupational exoskeletons: Overview of their benefits and limitations in preventing work-related musculoskeletal disorders, IISE Trans. Occup. Ergon. Hum. Factors (2019) 1–17.
[3] C. Bartneck, D. Kulić, E. Croft, S. Zoghbi, Measurement instruments for the anthropomorphism, animacy, likeability, perceived intelligence, and perceived safety of robots, Int. J. Soc. Robot. 1 (1) (2009) 71–81.
[4] N. Maclean, P. Pound, C. Wolfe, A. Rudd, Qualitative analysis of stroke patients' motivation for rehabilitation, BMJ 321 (7268) (2000) 1051–1054.
[5] J. Fink, Anthropomorphism and human likeness in the design of robots and human-robot interaction, in: International Conference on Social Robotics, Springer, 2012, pp. 199–208.
[6] G. Averta, C. Della Santina, G. Valenza, A. Bicchi, M. Bianchi, Exploiting upper-limb functional principal components for human-like motion generation of anthropomorphic robots, J. Neuroeng. Rehabil. 17 (2020) 1–15.
[7] N. Jarrassé, T. Proietti, V. Crocher, J. Robertson, A. Sahbani, G. Morel, A. Roby-Brami, Robotic exoskeletons: a perspective for the rehabilitation of arm coordination in stroke patients, Front. Hum. Neurosci. 8 (2014) 947.
[8] A. Frisoli, C. Loconsole, R. Bartalucci, M. Bergamasco, A new bounded jerk on-line trajectory planning for mimicking human movements in robot-aided neurorehabilitation, Robot. Auton. Syst. 61 (4) (2013) 404–415.
[9] A. Dragan, S. Srinivasa, Integrating human observer inferences into robot motion planning, Auton. Robots 37 (4) (2014) 351–368.
[10] B.R. Duffy, Anthropomorphism and the social robot, Robot. Auton. Syst. 42 (3–4) (2003) 177–190.
[11] N. Jarrassé, V. Crocher, G. Morel, A method for measuring the upper limb motion and computing a compatible exoskeleton trajectory, in: 2012 IEEE/RSJ International Conference on Intelligent Robots and Systems, IEEE, 2012, pp. 3461–3466.
[12] J. Beil, G. Perner, T. Asfour, Design and control of the lower limb exoskeleton KIT-EXO-1, in: 2015 IEEE International Conference on Rehabilitation Robotics, ICORR, IEEE, 2015, pp. 119–124.

[13] S. Kousidou, N. Tsagarakis, C. Smith, D. Caldwell, Task-orientated biofeedback system for the rehabilitation of the upper limb, in: 2007 IEEE 10th International Conference on Rehabilitation Robotics, IEEE, 2007, pp. 376–384.
[14] L. Pignolo, G. Dolce, G. Basta, L. Lucca, S. Serra, W. Sannita, Upper limb rehabilitation after stroke: ARAMIS a "robo-mechatronic" innovative approach and prototype, in: 2012 4th IEEE RAS & EMBS International Conference on Biomedical Robotics and Biomechatronics, BioRob, IEEE, 2012, pp. 1410–1414.
[15] C.G. Burgar, P.S. Lum, P.C. Shor, H.M. Van der Loos, Development of robots for rehabilitation therapy: The Palo Alto VA/Stanford experience, J. Rehabil. Res. Dev. 37 (6) (2000) 663–674.
[16] S. Ivaldi, O. Sigaud, B. Berret, F. Nori, From humans to humanoids: the optimal control framework, Paladyn J. Behav. Robot. 3 (2) (2012) 75–91.
[17] M. Johnson, K. Wisneski, J. Anderson, D. Nathan, R. Smith, Development of ADLER: The activities of daily living exercise robot, in: The First IEEE/RAS-EMBS International Conference on Biomedical Robotics and Biomechatronics, 2006, BioRob 2006, IEEE, 2006, pp. 881–886.
[18] F. Oldewurtel, M. Mihelj, T. Nef, R. Riener, Patient-cooperative control strategies for coordinated functional arm movements, in: 2007 European Control Conference, ECC, IEEE, 2007, pp. 2527–2534.
[19] T. Flash, N. Hogan, The coordination of arm movements: an experimentally confirmed mathematical model, J. Neurosci. 5 (7) (1985) 1688–1703.
[20] M. Guidali, M. Büchel, V. Klamroth, T. Nef, R. Riener, Trajectory planning in ADL tasks for an exoskeletal arm rehabilitation robot, in: Technically Assisted Rehabilitation: TAR 2009; 2nd European Conference, March 18–19, 2009 in Berlin; Proceedings, Deutsche Gesellschaft für Biomedizinische Technik, 2009.
[21] E. Nakano, H. Imamizu, R. Osu, Y. Uno, H. Gomi, T. Yoshioka, M. Kawato, Quantitative examinations of internal representations for arm trajectory planning: minimum commanded torque change model, J. Neurophysiol. 81 (5) (1999) 2140–2155.
[22] Y. Wada, Y. Kaneko, E. Nakano, R. Osu, M. Kawato, Quantitative examinations for multi joint arm trajectory planning—using a robust calculation algorithm of the minimum commanded torque change trajectory, Neural Netw. 14 (4–5) (2001) 381–393.
[23] T. Kang, J. He, S.I.H. Tillery, Determining natural arm configuration along a reaching trajectory, Exp. Brain Res. 167 (3) (2005) 352–361.
[24] J.F. Soechting, C.A. Buneo, U. Herrmann, M. Flanders, Moving effortlessly in three dimensions: does Donders' law apply to arm movement? J. Neurosci. 15 (9) (1995) 6271–6280.
[25] A. Biess, D.G. Liebermann, T. Flash, A computational model for redundant human three-dimensional pointing movements: integration of independent spatial and temporal motor plans simplifies movement dynamics, J. Neurosci. 27 (48) (2007) 13045–13064.
[26] A. Montagner, A. Frisoli, L. Borelli, C. Procopio, M. Bergamasco, M.C. Carboncini, B. Rossi, A pilot clinical study on robotic assisted rehabilitation in VR with an arm exoskeleton device, in: 2007 Virtual Rehabilitation, IEEE, 2007, pp. 57–64.
[27] M. Guidali, A. Duschau-Wicke, S. Broggi, V. Klamroth-Marganska, T. Nef, R. Riener, A robotic system to train activities of daily living in a virtual environment, Med. Biol. Eng. Comput. 49 (10) (2011) 1213.
[28] T. Nef, M. Guidali, R. Riener, ARMin III–arm therapy exoskeleton with an ergonomic shoulder actuation, Appl. Bionics Biomech. 6 (2) (2009) 127–142.
[29] A. Zeiaee, R. Soltani-Zarrin, R. Langari, R. Tafreshi, Design and kinematic analysis of a novel upper limb exoskeleton for rehabilitation of stroke patients, in: 2017 International Conference on Rehabilitation Robotics, ICORR, IEEE, 2017, pp. 759–764.
[30] P.D. Neilson, M.D. Neilson, R.T. Bye, A Riemannian geometry theory of human movement: The geodesic synergy hypothesis, Hum. Mov. Sci. 44 (2015) 42–72.
[31] M. Flanders, J.M. Hondzinski, J.F. Soechting, J.C. Jackson, Using arm configuration to learn the effects of gyroscopes and other devices, J. Neurophysiol. 89 (1) (2003) 450–459.
[32] R. Soltani-Zarrin, A. Zeiaee, R. Langari, N. Robson, Reference path generation for upper-arm exoskeletons considering scapulohumeral rhythms, in: 2017 International Conference on Rehabilitation Robotics, ICORR, IEEE, 2017, pp. 753–758.
[33] R. Soltani-Zarrin, A. Zeiaee, R. Langari, R. Tafreshi, A computational approach for human-like motion generation in upper limb exoskeletons supporting scapulohumeral rhythms, in: 2017 International Symposium on Wearable Robotics and Rehabilitation, WeRob, IEEE, 2017, pp. 1–2.
[34] X. Wang, M. Maurin, F. Mazet, N.D.C. Maia, K. Voinot, J.P. Verriest, M. Fayet, Three-dimensional modelling of the motion range of axial rotation of the upper arm, J. Biomech. 31 (10) (1998) 899–908.
[35] N. Klopčar, M. Tomšič, J. Lenarčič, A kinematic model of the shoulder complex to evaluate the arm-reachable workspace, J. Biomech. 40 (1) (2007) 86–91.
[36] A. Zeiaee, R. Soltani-Zarrin, R. Langari, R. Tafreshi, Kinematic design optimization of an eight degree-of-freedom upper-limb exoskeleton, Robotica 37 (12) (2019) 2073–2086.

Rana Soltani Zarrin received her B.Sc. degree in Electrical Engineering from University of Tabriz, the M.Sc. degree in Mechanical Engineering from University of Central Florida, and the Ph.D. degree in Mechanical Engineering from Texas A&M University in 2010, 2013, and 2019, respectively. Her research interests are collaborative robots, robot motion planning and control, human-robot interaction, dexterous manipulation, and computational neuroscience.

Amin Zeiaee received the B.Sc. degree in Electrical Engineering from University of Tabriz, the M.Sc. degree in Mechanical Engineering from University of Central Florida, and the Ph.D. degree in Mechanical Engineering from Texas A&M University in 2010, 2013 and 2019, respectively. His research interests are wearable robotics, physical human-robot interaction, nonlinear techniques for control of robotic manipualtors, and motion planning/control of input-constrained wheeled robots.

Reza Langari received the B.Sc., M.Sc., and Ph.D. degrees from University of California,Berkeley, CA, USA, in 1981, 1983, and 1991, respectively. He started his academic career with Texas A&M University, College Station, TX, USA, in September 1991. His expertise is in the area of computational intelligence, with application to mechatronic systems, industrial automation, and autonomous vehicles. He currently serves as the Editor-in-Chief of Journal of Intelligent and Fuzzy Systems.

John Buchanan is a professor in the department of Health and Kinesiology in Texas A&M University. He received his Ph.D. in Complex Systems and Brain Sciences from Florida Atlantic University in 1996. He was a postdoctoral fellow at the Neurological Sciences Institute of Oregon Health Sciences University before joining Texas A&M in May of 1999. His current research interests are in the area of bimanual motor control/learning, multijoint arm control, and observational learning of motor skills.

Nina Robson is an associate professor in the Department of Mechanical Engineering at California State University Fullerton. She holds an M.Sc. degree in Mechanical and Aeronautical Engineering from the University of California, Davis (2001) and a Ph.D. degree in Mechanical and Aerospace Engineering from the University of California, Irvine in 2008. Dr. Robson's current research interests are human motion planning with reduced mobility, robust robotic design, and biomechanics.